



# Imaging ultrafast evolution of subwavelength-sized topography using single-probe structured light microscopy

JIE XU,<sup>1</sup> CHANGJUN MIN,<sup>1,3</sup> YUQUAN ZHANG,<sup>1,4</sup> JIELEI NI,<sup>1</sup> GENGWEI CAO,<sup>1</sup> QIANYI WEI,<sup>1</sup> JIANJUN YANG,<sup>2</sup> AND XIAOCONG YUAN<sup>1,5</sup>

<sup>1</sup>Nanophotonics Research Center, Shenzhen Key Laboratory of Micro-Scale Optical Information Technology & Institute of Microscale Optoelectronics, Shenzhen University, Shenzhen 518060, China

<sup>2</sup>State Key Laboratory of Applied Optics, Changchun Institute of Optics, Fine Mechanics and Physics, Chinese Academy of Sciences, Changchun 130033, China

<sup>3</sup>e-mail: cjmin@szu.edu.cn

<sup>4</sup>e-mail: yqzhang@szu.edu.cn

<sup>5</sup>e-mail: xcyuan@szu.edu.cn

Received 17 March 2022; revised 20 June 2022; accepted 21 June 2022; posted 22 June 2022 (Doc. ID 458613); published 27 July 2022

Imaging ultrafast processes in femtosecond (fs) laser–material interactions such as fs laser ablation is very important to understand the physical mechanisms involved. To achieve this goal with high resolutions in both spatial and temporal domains, a combination of optical pump–probe microscopy and structured illumination microscopy can be a promising approach, but suffers from the multiple-frame method with a phase shift that is inapplicable to irreversible ultrafast processes such as ablation. Here, we propose and build a wide-field single-probe structured light microscopy (SPSLM) to image the ultrafast three-dimensional topography evolution induced by fs lasers, where only a single imaging frame with a single structured probe pulse is required for topography reconstruction, benefiting from Fourier transform profilometry. The second harmonic of the fs laser is used as the structured probe light to improve spatial lateral resolution into the subwavelength region of  $\sim 478$  nm, and the spatial axial and temporal resolutions are estimated to be  $\sim 22$  nm and  $\sim 256$  fs, respectively. With SPSLM, we successfully image the ultrafast topography evolution of a silicon wafer surface impacted by single and multiple fs pulses. The variable formation and evolution of the laser induced periodic surface structures during an ultrashort time are visualized and analyzed. We believe that SPSLM will be a significant approach for revealing and understanding various ultrafast dynamics, especially in fs laser ablation and material science. © 2022 Chinese Laser Press

<https://doi.org/10.1364/PRJ.458613>

## 1. INTRODUCTION

Femtosecond (fs) laser–material interactions lead to many interesting phenomena such as transient demagnetization of ferromagnets, fs laser filamentation, and isomerization of proteins [1–5]. Due to strong instantaneous power, fs lasers have been applied in various fields such as laser writing, reshaping, and ablation [6–8]. To reveal the ultrafast physical/chemical dynamic response in fs laser–material interactions and promote the applications of fs lasers, especially for application in laser fabrication, a powerful microscope that can capture the ultrafast process is urgently needed [9–11].

As a candidate, optical pump–probe microscopy, including types of near-field single-point scanning [12] and far-field wide-field imaging [13], has grown into a mature ultrafast imaging technique and been widely adopted in chemical reaction,

molecular dynamics, and others [14–19]. Compared to the single-point scanning type, the wide-field pump–probe microscope benefits from a much larger imaging area and faster imaging speed, therefore having proven advantages in investigating physical mechanisms and material properties in the fields of fs laser ablation and material science [20–24]. For example, by utilizing the wide-field pump–probe microscope, Fang *et al.* successfully visualized the evolution of the fs laser induced surface structural dynamics of metal through backscattered light [21], and Pan *et al.* studied the ultrafast reflectivity response and ablation mechanisms of molybdenum disulfide under intense fs laser irradiation [22].

However, most previously studied wide-field pump–probe microscopes can achieve only two-dimensional imaging and have low spatial resolutions in micrometer scale. To expand two-dimensional imaging to three-dimensional and improve

resolution, the combination of optical pump–probe microscopy and structured illumination microscopy (SIM) can be a promising approach [25], during which multiple sectional images with phase shifts are required [26–32]. However, under the condition that the damage threshold of the material is exceeded by the fs laser, it is impossible to guarantee that ultrafast processes in all repeated frames stay exactly the same. Final structures induced by different fs pulses are not perfectly the same, due to the fact that pump pulses influenced by air disturbance and other environmental factors are slightly different from each other. As a result, the multi-frame images obtained through imperfect repetition cannot reconstruct accurate sample images via the SIM algorithm. Hence, this kind of structured illumination pump–probe microscope cannot be applied to an irreversible ultrafast process during which physical/chemical properties of the sample are damaged, such as ablation.

To image fs laser induced irreversible ultrafast topography, a reconstruction method with a single frame is required instead of the common SIM. As a possible candidate, Fourier transform profilometry (FTP) is a 3D imaging technique that needs only one frame of the image [33–36], and has been widely used in macroscopical applications such as industrial inspection and machine vision [37–39]. Based on the triangulation method of geometrical optics [39], the height of a measured sample is considered linearly dependent on the phase calculated by FTP, and the 3D topography of the sample finally can be reconstructed [34]. Although FTP is also based on structured light illumination, it cannot achieve spatial super-resolution like SIM, but requires only a single shot of pulse and thus has great potential for imaging fs laser induced irreversible ultrafast topography. However, FTP is rarely used in optical microscopes with large numerical aperture (NA) objectives, where the sample size is too small and the spatial frequency is much higher than those in macroscopical applications. Under this condition, how to apply FTP to a high-NA microscope is still a challenge.

In this work, we propose and experimentally verify a single-probe structured light microscopy (SPSLM) that combines a pump–probe technique and wide-field structured light

microscopy associated with FTP. Benefitting from the advantage of FTP, our SPSLM requires only a single frame obtained by a single structured probe pulse for 3D topography reconstruction, and thus can be used to image the ultrafast evolution of topography on a material surface influenced by a fs laser. The second harmonic of the initial fs laser is modulated as structured probe light, improving the spatial lateral resolution into the subwavelength region of  $\sim 478$  nm (less than the laser central wavelength of 800 nm), and the spatial axial and temporal resolutions are estimated to be  $\sim 22$  nm and  $\sim 256$  fs, respectively. The reconstructed topography of samples from the proposed SPSLM agrees well with the results from an atomic force microscope (AFM), confirming the reliability of SPSLM and topography reconstruction methods. To demonstrate the application potential of this strategy, we apply SPSLM to image the ultrafast topography evolution on the surface of a monocrystalline silicon (Si) wafer impacted by single and multiple fs laser pulses with different pulse energies. Finally, variable formation and evolution processes of laser induced periodic surface structures (LIPSSs) are revealed and investigated by SPSLM.

## 2. SYSTEM AND METHODS

### A. Experimental Setup of SPSLM

The proposed SPSLM contains two subsystems, including a traditional pump–probe microscope subsystem and a structured light subsystem, as depicted in Fig. 1. The light source is an amplified Ti:sapphire laser system that generates 120 fs pulses with maximal energy of 3 mJ and a central wavelength of 800 nm. The initial pulse partially ( $\sim 20\%$ ) generates the second harmonics at 400 nm after passing through a  $\beta$ -barium borate (BBO) crystal and is reflected by a dichroic mirror (DM1) as a probe light, depicted in violet in Fig. 1. The fundamental light at 800 nm transmits through DM1 as a pump light, depicted in red in Fig. 1, and is selected into a single pulse by a fast electromechanical shutter. Both pump and probe lights are attenuated by tunable stepping filters. Aiming at measuring the effective energy of the pump pulse on the sample using a Joulemeter, a small aperture is used to make sure that all

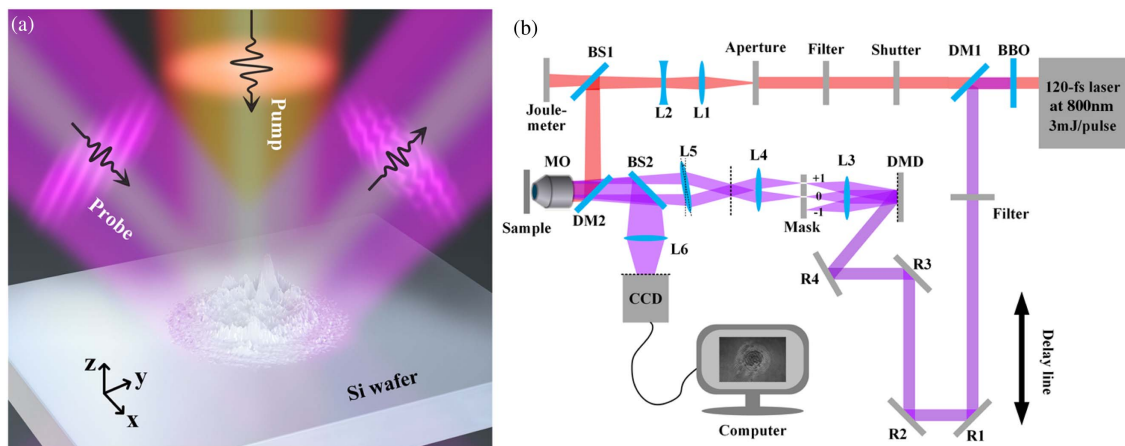


**Fig. 1.** Schematic of the SPSLM, where red and violet indicate pump light (at 800 nm) and probe light (at 400 nm), respectively. (a) Diagram of ultrafast pulses on Si wafer. (b) Optical path of SPSLM: BBO, barium boron oxide; DM1, DM2, dichroic mirrors; L1–L6, lenses; R1–R5, reflectors; BS1, BS2, beam splitters; DMD, digital mirror device; CCD, charge-coupled device; MO, microscope objective (100 $\times$ , apochromatic, NA = 0.9).

subsequent light enters the back aperture of the objective. We use two lenses (L1 and L2) after the aperture to change the divergence angle of the pump light. With this setup, the influenced area of the pump light on the sample is modified into a diffractive Airy spot instead of a focus point, having a measured diameter of  $\sim 12 \mu\text{m}$ . Both pump and probe beams are coupled into the back aperture of a  $100\times$  apochromatic microscope objective (MO, NA = 0.9) via DM2. The single pump pulse energy is varied from  $\sim 200 \text{ nJ}$  to  $\sim 400 \text{ nJ}$ , corresponding to an average fluence ranging from  $\sim 0.2 \text{ J/cm}^2$  to  $\sim 0.4 \text{ J/cm}^2$ , which is higher than the damage threshold of monocrystalline Si ( $0.17 \text{ J/cm}^2$ ) [40]. The energy fluence of the probe pulse is about  $0.01 \text{ J/cm}^2$ , much lower than the damage threshold of the material. An optical delay line is used to provide the desirable time delay between pump and probe lights, with a maximum value of 10 ns and minimum time step of 20 fs.

The most unique feature of SPSSLM is that the structured light subsystem is off-axis, which establishes the condition of a triangulation method for FTP. As shown in Fig. 1(b), the second-harmonic probe beam is directed toward the digital mirror device (DMD) to produce several diffraction orders. We select the +1st and zeroth orders by using a mask located at the confocal plane of the  $4f$ -system (L3 and L4). Lens L5 and MO constitute another  $4f$ -system to transmit the fs interference fringes formed by the +1st and zeroth orders on the sample. Because the pulses of +1st and zeroth orders have a small retardation in time domain on the plane perpendicular to the optical axis, lens L5 is slightly tilted to match their optical paths. Within this kind of off-axis optical system, the interference fringes formed by the +1st and zeroth orders obliquely illuminate on the sample, as schematically shown in Fig. 1(a). The reflected interference fringes carrying the topography information of the sample are collected through the same MO and imaged through another  $4f$ -system (MO and L6) on a CCD camera (GS3-U3-120S6M-C, FLIR). The exposure time of the camera is set to 100 ms, and the repetition rate of the fs laser is set to 10 Hz via the electromechanical shutter, so each frame captured by the CCD is the image generated by a single fs pulse. The actual exposure time is equivalent to the pulse width of the fs probe light. By adjusting the time delay between the pump light and probe light, ultrafast images at different time can be obtained. After passing through many optical devices, the overall efficiency of the second harmonic light used for the probe is less than 1%, and the signal-to-noise ratio is about nine, which was obtained by calculating the ratio of the fundamental power (signal) to the background frequency power (noise) in frequency domain. We precisely match the optical paths of pump and probe beams to make sure that the delay line contains a zero-point delay. Due to our limited experimental conditions, the pulse widths of the pump and probe lights on the sample surface cannot be measured experimentally, and thus we did some theoretical calculations. For the initial Gaussian transform-limited 120 fs (full width at half maximum) pulse of the laser source, both pump and probe pulses arriving on the sample surface are broadened and theoretically estimated to be about 147 fs and 256 fs, respectively, by calculating the overall dispersions in the optical paths [41]. Thus, the temporal resolution of the proposed SPSSLM is about

256 fs, restricted by the pulse width of the probe light. The temporal resolution could be further improved via the pulse shaping/compression module such as spatial light modulators, and pairs of prisms and gratings [42–44].

## B. Topography Reconstruction Method

The fundamental method we used for topography reconstruction is FTP, where only one frame of a structural-light-illuminated image is required. The principle of FTP is that the light fringes illuminating on a fluctuant sample surface are deformed, and the corresponding phase shift is dependent on the fluctuation amplitude. In traditional FTP, the phase shift of reflected fringes is approximately considered linearly dependent on the height of the measured surface [33–39]. The relationship can be obtained by macroscopic system parameters. For the high-NA objective used in our SPSSLM, these parameters are much smaller and difficult to be measured directly and accurately.

To calibrate this relationship, we evaluate the structured light subsystem alone by shutting the pump light and imaging a piece of polished monocrystal Si wafer (surface roughness  $< 2 \text{ nm}$ ) as shown in Fig. 2. Considering that both axial and lateral resolutions are obtained by the single frame in FTP with limited information, there is a trade-off between axial and lateral resolutions that can be controlled by the period of interference fringes. To achieve an acceptable resolution for the LIPSS sample in both axial and lateral directions, we conduct a large number of experiments and eventually choose the period of interference fringes on the sample as 478 nm, corresponding to 10 pixels on DMD. Under this condition, based on the principle of the FTP algorithm, the best lateral resolution ( $x$ - $y$  plane) of the FTP reconstructed image is about 478 nm, which equals the period of interference fringes on the sample. The field of view is chosen at the center region ( $18 \mu\text{m} \times 18 \mu\text{m}$ ) of the DMD image on the sample, where the interference fringes formed by the +1st and zeroth orders have high contrast, as shown in Figs. 2(a) and 2(b). Then we continuously move the Si wafer in  $z$  direction with a step of 20 nm and record images at all positions near the focal plane as shown in Fig. 2(b), until the fringe contrast is smaller than 0.2, which indicates out-of-focus for the Si surface. The total distance that the sample moves in the  $z$  direction with a fringe contrast  $> 0.2$  is about  $3 \mu\text{m}$ , indicating the measurement range in  $z$  direction. As shown in Fig. 2(c), the recorded fringes show a phase shift when the  $z$  position of the sample changes, and a phase shift of  $\pi$  approximately corresponds to the distance of 180 nm. We define the plane with the fringe contrast having the maximum value as the  $z = 0$  plane, and take the  $+z$  direction as the positive phase shift direction. Last, the relationship between the phase shift from  $z = 0$  and the position of the sample in the  $z$  axis is obtained and shown in Fig. 2(d). The relationship is approximately linear with slight deviation, which is mainly caused by aberration of the off-axis subsystem.

The initial phase obtained from FTP is limited within the range from  $-\pi$  to  $\pi$ , corresponding to the range of arctangent function. Hence, a phase jump would occur when the difference between the two adjacent phase values exceeds the range. Our subsequent algorithm includes an unwrapping part to expand the wrapped phase into a continuous phase as follows:

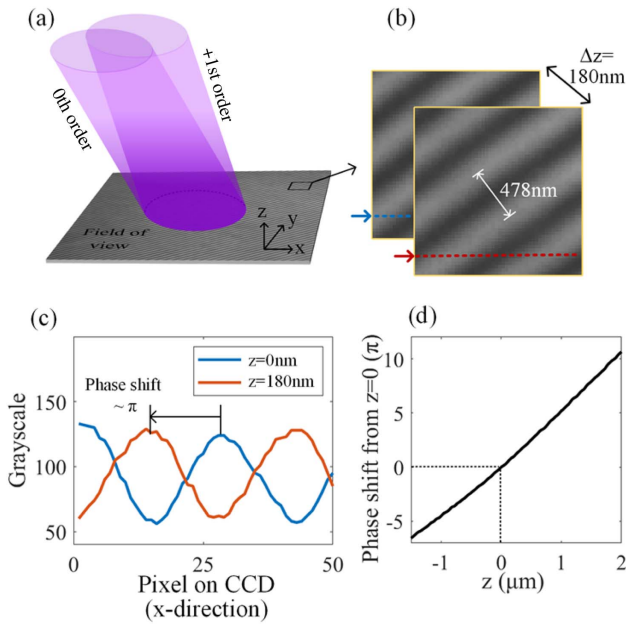


**Fig. 2.** Principle and calibration of topography reconstruction. (a) Schematic of illumination light on the field of view formed by interference of the +1st and zeroth orders; (b) fringes in raw image of a polished monocrystalline Si wafer (surface roughness <math><2\text{ nm}</math>) at different planes perpendicular to  $z$  axis; (c) grayscale distributions in  $x$  direction on CCD, with sample placed at  $z = 0\text{ nm}$  and  $z = 180\text{ nm}$ ; (d) phase shift from  $z = 0$  to various  $z$  positions, as a function of  $z$ , indicating the calibration between phase and height.

when the phase jump occurs, the algorithm adds  $2\pi k$  to each successive pixel and updates  $k$  at each phase jump, where  $k$  represents the serial number of the jump and starts from one. More detailed information of the unwrapping process can be obtained from Refs. [33–39].

Based on the calibration result, as well as the principle of the FTP algorithm and fringe period mentioned above, we can theoretically obtain the axial resolution ( $z$  direction) of SPSLM [34]. Since the phase shift of  $2\pi$  corresponds to both a period of 478 nm in lateral direction [Fig. 2(b)] and a distance of 360 nm in axial direction [Fig. 2(c)], and every pixel on CCD is measured to occupy about 30 nm on the sample plane, the single pixel on CCD also corresponds to  $(30/478) \times 360 \approx 22\text{ nm}$  in axial direction. A single pixel on CCD indicates the minimum stepping unit in frequency domain for FTP, so the axial resolution of SPSLM associated with the reconstruction algorithm is also about 22 nm.

To verify the reliability of the topography reconstruction method of FTP, we use a sample with distinctive features as shown in Fig. 3(a), which is a height map obtained via AFM. It is an ablation spot on the polished Si carbide induced by multiple fs laser pulses using our SPSLM, which contains a low-frequency pit and high-frequency LIPSS. The raw image of the sample via our structured light subsystem is shown in Fig. 3(b), and was calculated into a height map according to the FTP method. The reconstructed height map is shown in Fig. 3(c), using the same color bar as that obtained from AFM. It is obvious that both the low-frequency pit and

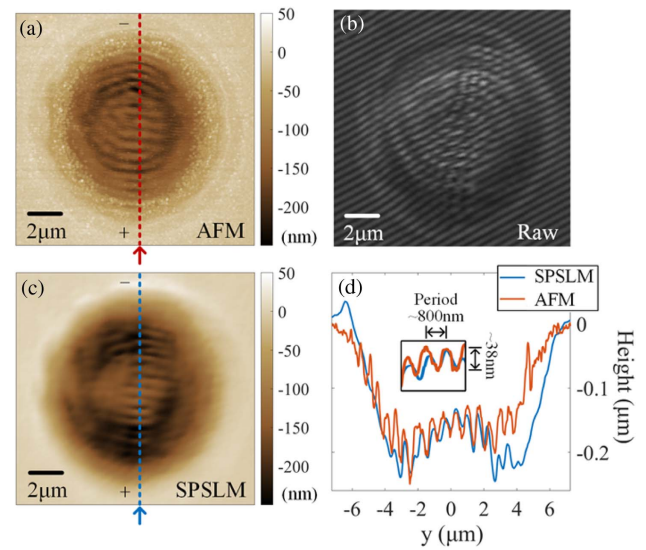


**Fig. 3.** Verification of topography reconstruction. (a) Height map of a sample (ablation point on the surface of a polished silicon carbide, containing a pit and LIPSS) obtained via AFM; (b) raw image obtained via SPSLM; (c) reconstructed topography from the raw image; (d) height variations along the dashed lines in (a) and (c) for comparison.

LIPSS are distinguishable and have almost the same morphology as that of AFM. More quantitative details across the center of the pit [along dashed lines in Figs. 3(a) and 3(c)] are shown in Fig. 3(d), including two curves from SPSLM and AFM for comparison. The height curve from SPSLM agrees well with that from AFM except that near the pit edge where the height is steeply raked. This deviation may be induced from the inherent limitation of FTP, which requires that the slope of the sample surface should not be too sharp [34]. The discrepancy on the right side ( $y = 2\text{--}6\ \mu\text{m}$ ) is due to the oblique illumination of the structured probe light, which leads to lower reflectivity and signal-to-noise ratio on this side, which affects FTP reconstruction. Nevertheless, the LIPSS with a period of  $\sim 800\text{ nm}$  and altitude intercept of 38 nm can be clearly distinguished via SPSLM. This result proves that our SPSLM system with the topography reconstruction method is effective and reliable.

### 3. RESULTS AND DISCUSSION

#### A. Single-Pulse Irradiation on Si Surface

To demonstrate the ultrafast surface imaging capability of SPSLM, the topography evolution of a monocrystalline Si surface induced by the fs laser is studied. To match the influenced area and the view field of SPSLM, the fs pump pulse obliquely impacts the sample, resulting in a slight time delay for different points on the wavefront arriving at the sample surface, as shown in Fig. 4. The raw images in the first row are captured via SPSLM at different time delays with a temporal step of 0.5 ps between the structured probe pulse and the single pump pulse controlled by the optical delay line. We can observe that the reflectivity on the left side first increases (becomes brighter), and then the bright area expands to a full circle of the pump

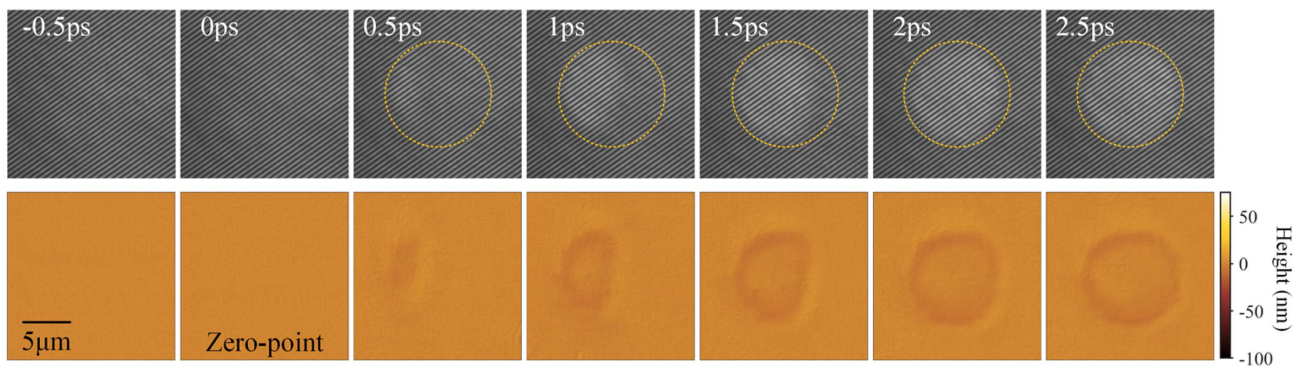


**Fig. 4.** Raw images (first row) and reconstructed height maps (second row) in time sequence near the zero point with the step of 0.5 ps captured by SPSLM. Pump pulse impacts on Si wafer in the area in orange dashed circle, with average fluence of about  $0.29 \text{ J/cm}^2$ .

pulse area at a time delay of about 2.5 ps. The orange dashed circle indicates the pump pulse area on the Si wafer. The increase in reflectivity in this area is due to the high-density plasma excited by the pump pulse [40,45,46]. This effect can be adaptable to set the zero point at the time delay when the increase in reflectivity begins, as Refs. [20,40] point out.

The second row in Fig. 4 shows the reconstructed height maps in time sequence corresponding to the raw images in the first row, by using the SPSLM associated with the FTP topography reconstruction algorithm. It can be seen that, in addition to the change of reflectivity, the surface morphology also changes at the same time. When the ultrashort pump pulse impacts the Si wafer, high-energy free electrons are generated and subsequently have scattering with the lattice via phonons in an ultrashort time scale, leading to the slight morphological change of the Si wafer surface, as shown by a shallow pit in Fig. 4. As the pit center is flat, fringes are slightly distorted mainly at the pit boundary in the first row of Fig. 4.

The topography evolutions on the Si surface impacted by the single pump pulse with various energies are obtained as

shown in Fig. 5. The pulse energy cases of 266 nJ, 304 nJ, and 382 nJ are denoted as “energies 1–3,” respectively. Results at six time delays of 5 ps, 40 ps, 100 ps, 1 ns, 4 ns, and 10 ns are given. The time delay of the final result at the time delay of 100 ms is denoted as “ $\infty$ ” because it is long enough to achieve the equilibrium state for the ultrafast dynamics on the Si surface. Since the ablation area of the pump light is about  $105 \mu\text{m}^2$ , the average fluence values for energies 1–3 are  $0.23 \text{ J/cm}^2$ ,  $0.29 \text{ J/cm}^2$ , and  $0.34 \text{ J/cm}^2$ , respectively, all of which are higher than the damage threshold of  $0.17 \text{ J/cm}^2$ . As mentioned in Section 2.A, the pump light is an Airy spot on the sample plane, which means that the energy fluence at the center is much higher than the average value, but the energy fluence at the spot edge is relatively lower. It leads to the phenomenon that the topography at the spot center changes much more dramatically than that near the spot edge, which can be observed in Fig. 5, especially for energy 3.

In the case of energy 3, a high region (bright color) occurs in the ablation area at the time delay of 40 ps, and then splits into a smaller disk region (indicated as a red arrow) and an annular

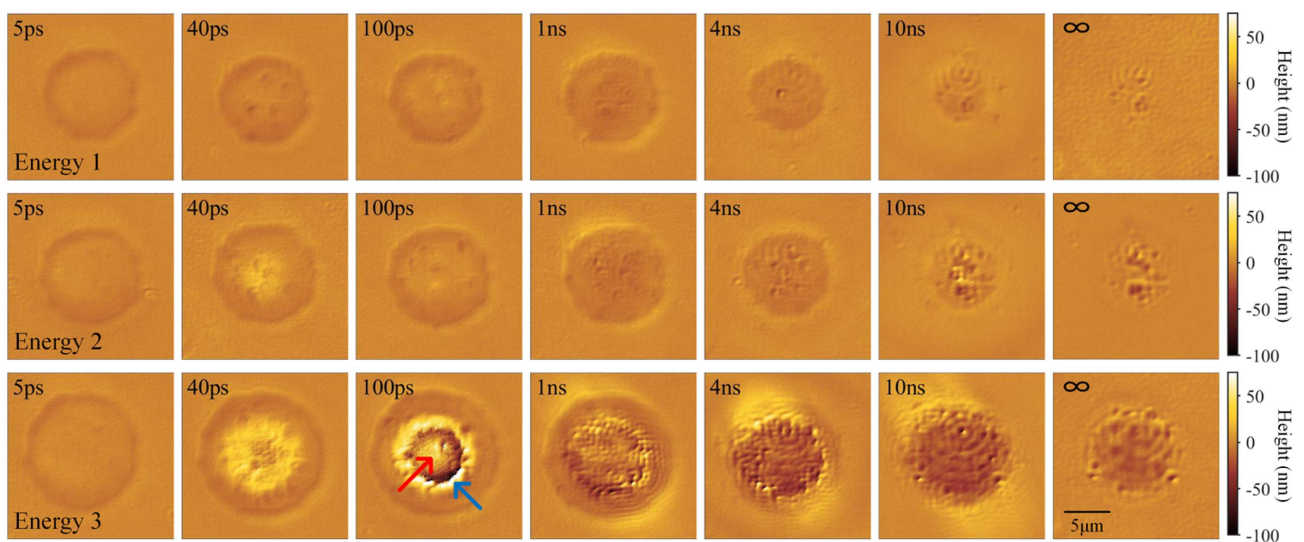


**Fig. 5.** Ultrafast evolution of the topography on Si surface impacted by a single pump pulse with different energies of 266 nJ, 304 nJ, and 382 nJ, corresponding to the average fluences of  $0.23 \text{ J/cm}^2$ ,  $0.29 \text{ J/cm}^2$ , and  $0.34 \text{ J/cm}^2$ , respectively (see Visualization 1). The pump light is linearly polarized in the horizontal direction. The final result at a time delay of 100 ms is denoted as “ $\infty$ .” All other parameters are the same as those in Fig. 4.

(blue arrow) region at the time of 100 ps. These two regions interact with each other to form ripples at the time delay around 1 ns, then the amplitude of ripples decreases, and a pit begins to appear at the time delay of 4 ns. By comparing the final topography and that at the time delay of 10 ns, we find that they have similar structures, but the pit has shallower depth finally, which means some changes occur after 10 ns, as the results in Refs. [20,21] indicate, but beyond the measurement range of our optical delay line. In addition, the final topography maps under energies 1–3 indicate that the pulse energy is an important parameter, and lower energy leads to shallower and smaller structures. More detailed processes of the topography evolution of the Si wafer surface for energies 1–3 are given in Visualization 1.

### B. Multi-pulse Irradiation on Si Surface

An interesting phenomenon in fs laser–material interaction is the formation of LIPSS, on which numerous studies have been reported [47–50]. However, both the morphological responses and topography evolution during the ultrafast process are rarely studied, which are of great significance for understanding of the

underlying mechanisms of LIPSS. By employing our SPSSLM system, we have realized the LIPSS formation and its ultrafast topography evolution dynamics, as shown in Fig. 6. The sample is also a Si wafer, but with the impact of multiple laser pulses with identical energies in time sequence. The repetition rate of the pump light is set to be 10 Hz, corresponding to 100 ms time intervals of neighboring pulses. Specifically, we investigate the ultrafast topography evolution after the second and third pump pulses impacting the final topography results in Fig. 5 induced by the first pump pulse. All pump pulses are linearly polarized in the horizontal direction. Other parameters are the same as those in Fig. 5 except for the range of the color bar, with the consideration that multiple laser pulses lead to a greater change in topography. Considering every two rows as a group, the three groups in Fig. 6 correspond to energies 1–3, respectively.

As clearly displayed in Fig. 6, after the successive second and third pulses impact the structures induced by the first pulse, LIPSS phenomena begin to appear with the spatial orientation perpendicular to the direction of the linear polarization of the

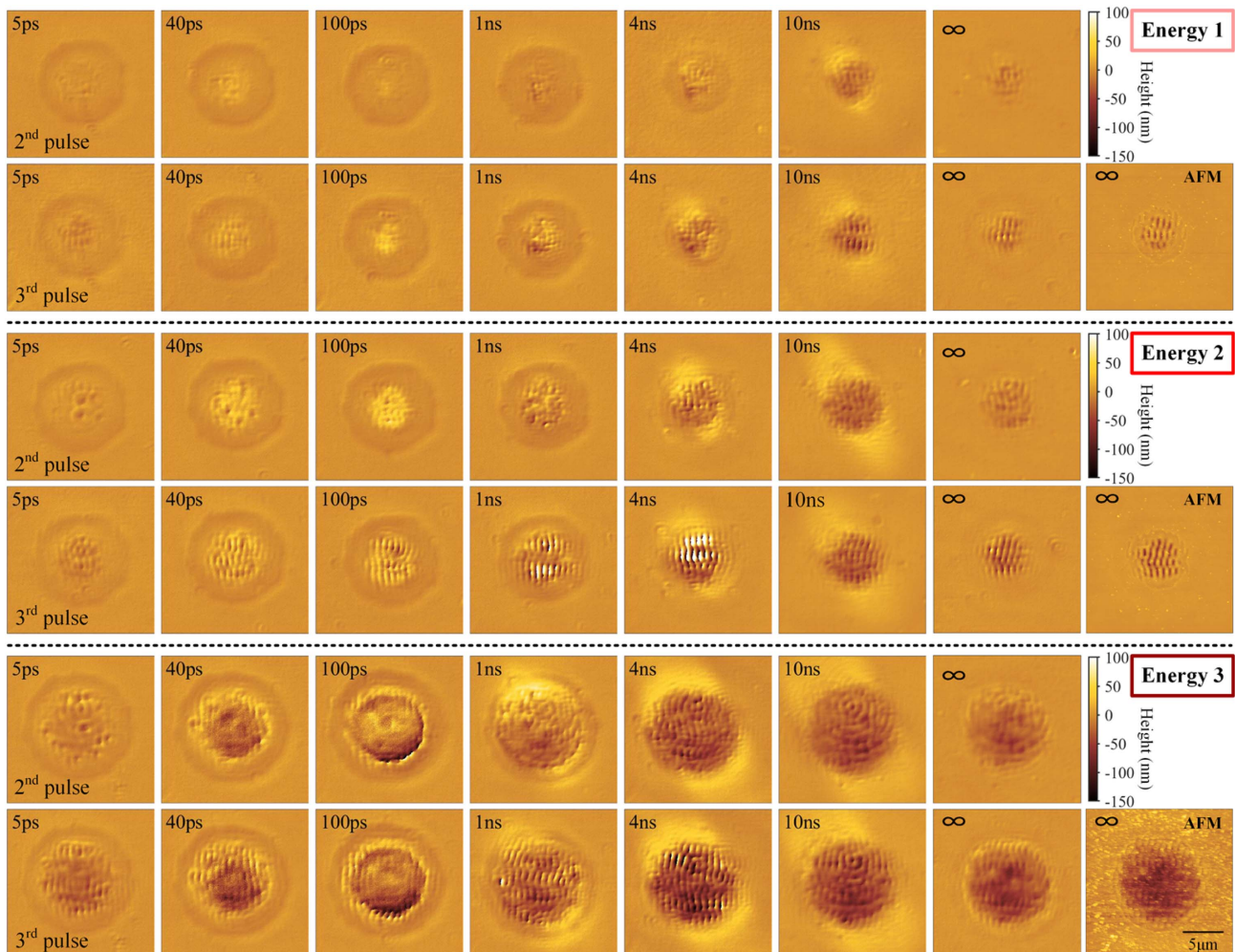


**Fig. 6.** Ultrafast topography evolution on the Si surface impacted by second and third pulses (see Visualization 1), and final results compared with AFM. Pulse energy in three groups (separated with black dashed lines) is the same as energies 1–3 in Fig. 5. Pump light is linearly polarized in horizontal direction. Final height maps obtained from SPSSLM and from AFM are given for comparison. All other parameters are the same as those in Fig. 5.

pump light. For the high-energy case of energy 3, the observation of LIPSSs shows the complex changes during the time delay ranging from 5 ps to 10 ns. As shown in the fifth row of Fig. 6, the LIPSSs first appear at 40 ps after the second pulse and form an annular region of periodic structures at 100 ps. Then the structured region spreads to the pit center at 1 ns and becomes clearer at 4 ns. However, at 10 ns and 100 ns after the second pulse, the LIPSSs gradually vanish, or at least, become not obvious. This trend of the topography evolution also occurs after the third pulse, as shown in the sixth row of Fig. 6. Last, some LIPSSs remain near the edge of the ablation spot, and a pit remains at the center. On the contrary, under the moderate case of energy 2, the pit center region contains obvious LIPSSs instead of a pit, as shown by the final result in the fourth row of Fig. 6. For the case of energy 2, the topography evolution is simpler than that under energy 3, that is, the LIPSSs are not clear after the second pulse, but become obvious during the whole ultrashort time after the third pulse. Especially at 1 ns and 4 ns, the altitude intercepts of LIPSSs are so great that they exceed the range of the color bar. For the low-energy case of energy 1, an interesting feature observed is that the LIPSSs appear after the third pulse at 5 ps, 40 ps, and 10 ns, but vanish at intermediate time delays of 100 ps, 1 ns, and 4 ns, as the second row of Fig. 6 shows. This phenomenon indicates the reorganization of LIPSSs during the intermediate time delay range.

The final state of LIPSSs is significant for applications such as fabrication of large-scale subwavelength gratings [51–54]. Final topography results after the third pulse obtained from SPSLM and from AFM are compared in Fig. 6. In all three energy cases, the low-frequency pit and high-frequency LIPSSs can be distinguished correctly. Results of energies 1 and 2 from SPSLM agree well with those from AFM, further proving that our SPSLM and the reconstruction method are effective and reliable. Under the situation of energy 3, the height map from AFM shows the generation of numerous nanoparticles around the ablation spot; however, they are out of resolution for SPSLM and unable to be distinguished.

Final states of topography after the third pulse in Fig. 6 also indicate that the formation of LIPSSs is closely related to the energy fluence of the pump pulse. Because of the pump pulse showing an Airy spot, the energy fluence is high in the pit center yet low near the edge, which indicates the energy fluence dependent formation of LIPSSs. For example, LIPSSs appear only in the center region for a pump pulse with lower energy fluence (energy 1 in Fig. 6), and the LIPSS region becomes larger when the pulse energy increases, as shown by the results under energy 2 in Fig. 6. For case of higher pulse energy (energy 3), LIPSSs in the pit center region are indistinct but clear near the edges. These phenomena indicate that the laser energy fluence needs to be appropriately controlled to achieve high-quality LIPSSs.

To quantify the quality of LIPSSs, we calculate the fast Fourier transformation (FFT) of the topography map and obtain the FFT power spectrum. Considering that LIPSSs appear mainly in the center region for energies 1 and 2 as shown in Fig. 6, only the center region of about  $3\ \mu\text{m} \times 3\ \mu\text{m}$  is investigated as an example. The FFT process is shown in Fig. 7, in

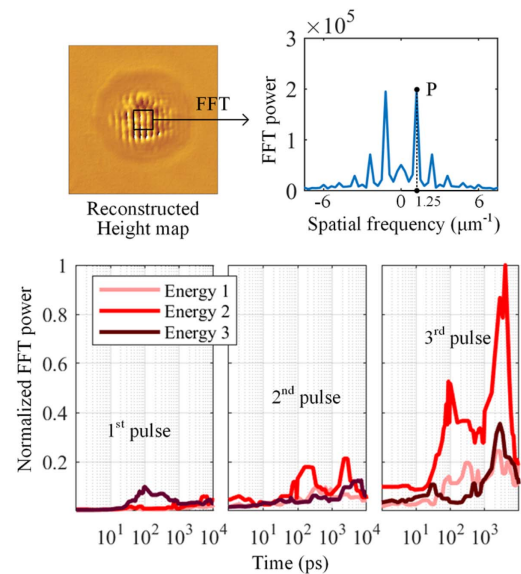


**Fig. 7.** Process of FFT to evaluate the quality of LIPSS located in the center region (about  $3\ \mu\text{m} \times 3\ \mu\text{m}$ ), and the variations of normalized FFT power of point  $P$  as a function of time delay after first, second, and third pulses, including the three cases of energies 1–3 (see Visualization 1).

which point  $P$  in the spatial frequency spectrum indicates the spatial frequency of LIPSSs with a period of 800 nm, which agrees well with many previous reports [47–54]. Thus, the FFT power at point  $P$  can be used to quantify the quality of LIPSSs in this region. With this method, we obtain variation of the normalized FFT power of point  $P$  as a function of time delay after impacts of the three pulses, as shown in Fig. 7. For the case of the first pulse, the most obvious feature is that the curve of energy 3 has a relatively high value during a time delay range from 100 ps to 1 ns. This effect results from the ripples formed by the disk region and annular region indicated by red and blue arrows in Fig. 5, respectively. For the cases of second and third pulses, the curve of energy 2 is much greater than those of energies 1 and 3, because the laser energy fluence of energy 2 is just in the appropriate range for the formation of high-quality LIPSSs. It must be pointed out, however, that we evaluate just the energy fluence effect in our specific experiments. According to Refs. [48–50], not only is laser energy fluence an important factor for the fabrication of high-quality LIPSSs, but also the pulse repetition rate and laser intensity distribution have great influence on the quality of LIPSSs. Another significant feature in Fig. 7 is that the curve of energy 2 shows two peaks around time delays of 100 ps and 3 ns for cases of both second and third pulses, indicating the reorganization of LIPSSs during the time delay range. More detailed information of the topography evolution of the Si wafer surface after first, second, and third pulses for the cases of energies 1–3 is given in Visualization 1.

#### 4. CONCLUSION

A wide-field SPSLM system is proposed and experimentally verified to image the ultrafast topography evolution induced

by fs laser pulses. The FTP method is introduced in SPSLM for ultrafast topography reconstruction with only a single imaging frame, and the relationship between phase and height has been studied and calibrated. The second harmonic of the initial fs laser is chosen as the probe light to generate the interference fringes on the sample surface, resulting in a spatial lateral resolution of  $\sim 478$  nm, axial resolution of  $\sim 22$  nm, and temporal resolution of  $\sim 256$  fs for SPSLM. Reconstructed topographies of samples via SPSLM and AFM agree well with each other, proving that our SPSLM and the topography reconstruction method are effective and reliable. To demonstrate the spatio-temporal imaging capability of SPSLM, we investigate the ultrafast topography evolution on the surface of a monocrystalline Si wafer influenced by single and multiple fs pulses. The ultrafast formation and evolution of the LIPSS have been successfully observed with appropriate fluence of a pump pulse. The reorganization of LIPSSs is found to occur during a time range from 100 ps to 3 ns after second and third pulses.

As final remarks, we note that the proposed SPSLM can be further developed to achieve better performance in the future. For example, although currently the lateral resolution of SPSLM cannot break through the diffraction limit of second harmonic light due to the single-frame reconstruction method, the spatial resolution can be further improved through deep learning, and the temporal resolution can also be improved by using a shorter pulse source or pulse compression methods. SPSLM also has potential in imaging internal ultrafast processes in transparent materials by modulating 3D structured probe light. We believe that SPSLM is not only a powerful tool for visualizing and understanding the ultrafast dynamics in fs laser–material interactions, but also has bright application prospects in various fields including laser fabrication, 3D printing, and material science.

**Funding.** Guangdong Major Project of Basic and Applied Basic Research (2020B0301030009); National Natural Science Foundation of China (62175157, 61935013, 61975128, 62005175); Leading Talents of Guangdong Province (00201505); Natural Science Foundation of Guangdong Province (2019TQ05X750); Shenzhen Science and Technology Program (JCYJ20210324120403011, KQTD20170330110444030, RCJC20210609103232046); Jilin Provincial Science & Technology Development Project (20200201086JC).

**Acknowledgment.** We thank Professor Jindong Tian for algorithm support. The authors acknowledge the Photonics Center of Shenzhen University for technical support.

**Disclosures.** The authors declare no conflicts of interest.

**Data Availability.** Data underlying the results presented in this paper are not publicly available at this time but may be obtained from the authors upon reasonable request.

## REFERENCES

1. P. Tengdin, W. You, C. Chen, X. Shi, D. Zusin, Y. Zhang, C. Gentry, A. Blonsky, M. Keller, and P. M. Oppeneer, "Critical behavior within 20 fs drives the out-of-equilibrium laser-induced magnetic phase transition in nickel," *Sci. Adv.* **4**, eaap9744 (2018).
2. P. Q. Elias, N. Severac, J. M. Luysen, Y. B. André, I. Doudet, B. Wattellier, J. P. Tobeli, S. Albert, and B. Mahieu, "Improving super-sonic flights with femtosecond laser filamentation," *Sci. Adv.* **4**, eaau5239 (2018).
3. K. Pande, C. D. M. Hutchison, G. Groenhof, A. Aquila, J. S. Robinson, J. Tenboer, S. Basu, S. Boutet, D. P. DePonte, and M. Liang, "Femtosecond structural dynamics drives the trans/cis isomerization in photoactive yellow protein," *Science* **352**, 725–729 (2016).
4. A. Y. Vorobyev and C. Guo, "Femtosecond laser nanostructuring of metals," *Opt. Express* **14**, 2164–2169 (2006).
5. Z. Lin, L. Ji, and M. Hong, "Enhancement of femtosecond laser-induced surface ablation via temporal overlapping double-pulse irradiation," *Photon. Res.* **8**, 271–278 (2020).
6. J. Boisvert, A. Hlil, S. Loranger, A. Riaz, Y. Ledemi, Y. Messaddeq, and K. Raman, "Photosensitization agents for fs laser writing in PDMS," *Sci. Rep.* **12**, 1623 (2022).
7. G. González-Rubio, P. Díaz-Núñez, A. Rivera, A. Prada, G. Tardajos, J. González-Izquierdo, L. Bañares, P. Llombart, L. G. Macdowell, and M. A. Palafox, "Femtosecond laser reshaping yields gold nanorods with ultranarrow surface plasmon resonances," *Science* **358**, 640–644 (2017).
8. N. Zhang, X. Zhu, J. Yang, X. Wang, and M. Wang, "Time-resolved shadowgraphs of material ejection in intense femtosecond laser ablation of aluminum," *Phys. Rev. Lett.* **99**, 167602 (2007).
9. P. Ding, Y. Yao, D. Qi, C. Yang, F. Cao, Y. He, J. Yao, C. Jin, Z. Huang, and L. Deng, "Single-shot spectral-volumetric compressed ultrafast photography," *Adv. Photon.* **3**, 045001 (2021).
10. Y. Yao, Y. He, D. Qi, F. Cao, J. Yao, P. Ding, C. Jin, X. Wu, L. Deng, and T. Jia, "Single-shot real-time ultrafast imaging of femtosecond laser fabrication," *ACS Photon.* **8**, 738–744 (2021).
11. X. Zeng, S. Zheng, Y. Cai, Q. Lin, J. Liang, X. Lu, J. Li, W. Xie, and S. Xu, "High-spatial-resolution ultrafast framing imaging at 15 trillion frames per second by optical parametric amplification," *Adv. Photon.* **2**, 056002 (2020).
12. V. Kravtsov, R. Ulbricht, J. M. Atkin, and M. B. Raschke, "Plasmonic nanofocused four-wave mixing for femtosecond near-field imaging," *Nat. Nanotechnol.* **11**, 459–464 (2016).
13. G. Spletor, D. Kilbane, A. K. Mahro, B. Frank, S. Ristok, L. Gal, P. Kahl, D. Podbiel, S. Mathias, and H. Giessen, "Revealing the subfemtosecond dynamics of orbital angular momentum in nanoplasmonic vortices," *Science* **355**, 1187–1191 (2017).
14. M. C. Fischer, J. W. Wilson, F. E. Robles, and W. S. Warren, "Invited review article: pump-probe microscopy," *Rev. Sci. Instrum.* **87**, 031101 (2016).
15. P. Dong and J. Cheng, "Pump-probe microscopy: theory, instrumentation, and applications," *Spectroscopy* **32**, 2–11 (2017).
16. M. Domke, S. Rapp, M. Schmidt, and H. P. Huber, "Ultrafast pump-probe microscopy with high temporal dynamic range," *Opt. Express* **20**, 10330–10338 (2012).
17. J. Yu, W. S. Warren, and M. C. Fischer, "Visualization of vermilion degradation using pump-probe microscopy," *Sci. Adv.* **5**, eaaw3136 (2019).
18. Y. Yu, X. Zhang, Z. Zhou, Z. Zhang, Y. Bao, H. Xu, L. Lin, Y. Zhang, and X. Wang, "Microscopic pump-probe optical technique to characterize the defect of monolayer transition metal dichalcogenides," *Photon. Res.* **7**, 711–721 (2019).
19. Y. Tan, H. Zhao, R. Zhang, Y. Zhao, C. Zhang, X. Zhang, and L. Zhang, "Transient evolution of quasifree electrons of plasma in liquid water revealed by optical-pump terahertz-probe spectroscopy," *Adv. Photon.* **3**, 015002 (2021).
20. J. Bonse, G. Bachelier, J. Siegel, and J. Solis, "Time- and space-resolved dynamics of melting, ablation, and solidification phenomena induced by femtosecond laser pulses in germanium," *Phys. Rev. B* **74**, 134106 (2006).
21. R. Fang, A. Vorobyev, and C. Guo, "Direct visualization of the complete evolution of femtosecond laser-induced surface structural dynamics of metals," *Light Sci. Appl.* **6**, e16256 (2017).
22. C. Pan, L. Jiang, J. Sun, Q. Wang, F. Wang, K. Wang, Y. Lu, Y. Wang, L. Qu, and T. Cui, "Ultrafast optical response and ablation

- mechanisms of molybdenum disulfide under intense femtosecond laser irradiation," *Light Sci. Appl.* **9**, 80 (2020).
23. T. Pflug, M. Olbrich, J. Winter, J. Schille, U. Löschner, H. Huber, and A. Horn, "Fluence-dependent transient reflectance of stainless steel investigated by ultrafast imaging pump-probe reflectometry," *J. Phys. Chem. C* **125**, 17363–17371 (2021).
  24. T. Feng, G. Chen, H. Han, and J. Qiao, "Femtosecond-laser-ablation dynamics in silicon revealed by transient reflectivity change," *Micromachines* **13**, 14 (2022).
  25. E. S. Massaro, A. H. Hill, and E. M. Grumstrup, "Super-resolution structured pump-probe microscopy," *ACS Photon.* **3**, 501–506 (2016).
  26. Y. Kim and P. T. C. So, "Three-dimensional wide-field pump-probe structured illumination microscopy," *Opt. Express* **25**, 7369–7391 (2017).
  27. M. A. A. Neil, R. Juškaitis, and T. Wilson, "Method of obtaining optical sectioning by using structured light in a conventional microscope," *Opt. Lett.* **22**, 1905–1907 (1997).
  28. C. Wang, K. Lee, and C. Lee, "Wide-field optical nanoprofilometry using structured illumination," *Opt. Lett.* **34**, 3538–3540 (2009).
  29. D. Dan, B. Yao, and M. Lei, "Structured illumination microscopy for super-resolution and optical sectioning," *Chin. Sci. Bull.* **59**, 1291–1307 (2014).
  30. T. Zhao, Z. Wang, T. Chen, M. Lei, B. Yao, and P. R. Bianco, "Advances in high-speed structured illumination microscopy," *Front. Phys.* **9**, 672555 (2021).
  31. P. Kner, B. B. Chhun, E. R. Griffis, L. Winoto, and M. G. L. Gustafsson, "Super-resolution video microscopy of live cells by structured illumination," *Nat. Methods* **6**, 339–342 (2009).
  32. C. Ling, C. Zhang, M. Wang, F. Meng, L. Du, and X. Yuan, "Fast structured illumination microscopy via deep learning," *Photon. Res.* **8**, 1350–1359 (2020).
  33. X. Su and Q. Zhang, "Dynamic 3-D shape measurement method: a review," *Opt. Laser Eng.* **48**, 191–204 (2010).
  34. X. Su and W. Chen, "Fourier transform profilometry: a review," *Opt. Laser Eng.* **35**, 263–284 (2001).
  35. M. Takeda and K. Mutoh, "Fourier transform profilometry for the automatic measurement of 3-D object shapes," *Appl. Opt.* **22**, 3977–3982 (1983).
  36. L. Chen, X. Nguyen, F. Zhang, and T. Lin, "High-speed Fourier transform profilometry for reconstructing objects having arbitrary surface colours," *J. Opt.* **12**, 095502 (2010).
  37. T. Tao, Q. Chen, J. Da, S. Feng, Y. Hu, and C. Zuo, "Real-time 3-D shape measurement with composite phase-shifting fringes and multi-view system," *Opt. Express* **24**, 20253–20269 (2016).
  38. P. Yao, S. Gai, Y. Chen, W. Chen, and F. Da, "A multi-code 3D measurement technique based on deep learning," *Opt. Laser Eng.* **143**, 106623 (2021).
  39. F. Chen, G. M. Brown, and M. Song, "Overview of 3-D shape measurement using optical methods," *Opt. Eng.* **39**, 10–22 (2000).
  40. J. Liu, X. Jia, W. Wu, K. Cheng, D. Feng, S. Zhang, Z. Sun, and T. Jia, "Ultrafast imaging on the formation of periodic ripples on a Si surface with a prefabricated nanogroove induced by a single femtosecond laser pulse," *Opt. Express* **26**, 6302–6315 (2018).
  41. M. Kolesik, J. Brown, and A. Bahl, "Modeling of ultrafast laser pulse propagation," *Proc. SPIE* **9835**, 983510 (2016).
  42. A. M. Weiner, "Ultrafast optical pulse shaping: a tutorial review," *Opt. Commun.* **284**, 3669–3692 (2011).
  43. A. M. Weiner, "Femtosecond pulse shaping using spatial light modulators," *Rev. Sci. Instrum.* **71**, 1929–1960 (2000).
  44. T. H. Dou, R. Tautz, X. Gu, G. Marcus, T. Feurer, F. Krausz, and L. Veisz, "Dispersion control with reflection gratings of an ultra-broadband spectrum approaching a full octave," *Opt. Express* **18**, 27900–27909 (2010).
  45. M. C. Downer, R. L. Fork, and C. V. Shank, "Femtosecond imaging of melting and evaporation at a photoexcited silicon surface," *J. Opt. Soc. Am. B* **2**, 595–599 (1985).
  46. R. Gunnella, G. Zgrablic, E. Giangrisostomi, F. D'Amico, E. Principi, C. Masciovecchio, A. Di Cicco, and F. Parmigiani, "Ultrafast reflectivity dynamics of highly excited Si surfaces below the melting transition," *Phys. Rev. B* **94**, 155427 (2016).
  47. S. He, J. J. Nivas, K. K. Anoop, A. Vecchione, M. Hu, R. Bruzzese, and S. Amoroso, "Surface structures induced by ultrashort laser pulses: formation mechanisms of ripples and grooves," *Appl. Surf. Sci.* **353**, 1214–1222 (2015).
  48. A. V. Dostovalov, K. A. Okotrub, K. A. Bronnikov, V. S. Terentyev, V. P. Korolkov, and S. A. Babin, "Influence of femtosecond laser pulse repetition rate on thermochemical laser-induced periodic surface structures formation by focused astigmatic Gaussian beam," *Laser Phys. Lett.* **16**, 026003 (2019).
  49. Y. Fuentes-Edfuf, J. A. Sanchez-Gil, C. Florian, V. Giannini, J. Solis, and J. Siegel, "Surface plasmon polaritons on rough metal surfaces: role in the formation of laser-induced periodic surface structures," *ACS Omega* **4**, 6939–6946 (2019).
  50. Y. Zhang, Q. Jiang, K. Cao, T. Chen, K. Cheng, S. Zhang, D. Feng, T. Jia, Z. Sun, and J. Qiu, "Extremely regular periodic surface structures in a large area efficiently induced on silicon by temporally shaped femtosecond laser," *Photon. Res.* **9**, 839–847 (2021).
  51. E. Skoulas, A. C. Tasolamprou, G. Kenanakis, and E. Stratakis, "Laser induced periodic surface structures as polarizing optical elements," *Appl. Surf. Sci.* **541**, 148470 (2021).
  52. S. Lechago, C. García-Meca, A. Griol, M. Kovylyna, L. Bellieres, and J. Martí, "All-silicon on-chip optical nanoantennas as efficient interfaces for plasmonic devices," *ACS Photon.* **6**, 1094–1099 (2019).
  53. C. Florian, S. V. Kimer, J. Krüger, and J. Bonse, "Surface functionalization by laser-induced periodic surface structures," *J. Laser Appl.* **32**, 022063 (2020).
  54. A. Y. Vorobyev and C. Guo, "Multifunctional surfaces produced by femtosecond laser pulses," *J. Appl. Phys.* **117**, 033103 (2015).